



# Unraveling the electronic structure of cobalt oxide nanoislands on Au(111)

Andreas Ørsted <sup>\*</sup>, Sebastian Vestergaard Salling, and Lars Diekhöner <sup>†</sup>

*Department of Materials and Production, Aalborg University, Skjernvej 4a, 9220 Aalborg, Denmark*



(Received 4 August 2023; accepted 16 October 2023; published 26 October 2023)

This study utilizes spatially resolved low-temperature scanning tunneling microscopy and spectroscopy to investigate cobalt oxide nanoislands on Au(111) single-crystal surfaces. The electronic structure of bilayer, trilayer, and multilayer islands is measured, and the findings are correlated with structural variations across the islands, at oxygen defect lines on the islands, and at the island step edges. Of particular importance is the identification of electronic features below the Fermi level unique to certain island edges that are well-known to exhibit increased chemical reactivity. The results advance the understanding of the electronic properties of surface-supported cobalt oxide nanostructures, which are known to be important for catalytic applications. Furthermore, on the trilayer island structures a distinct peak in the density of states at the Fermi level is measured that adds to theoretical predictions of superconductivity in CoO<sub>2</sub> layers.

DOI: [10.1103/PhysRevB.108.165424](https://doi.org/10.1103/PhysRevB.108.165424)

## I. INTRODUCTION

Cobalt oxide based materials have been seen to display many interesting properties in the fields of superconductivity, magnetism, electron transport, and heterogeneous catalysis [1–3]. One chemical process which is receiving increasing attention is that of water splitting, and the development of catalysts reducing the energy cost of the oxygen evolution reaction (OER), involved in the water splitting process, is of particular interest. To this end, there has been a focus on designing cheap, effective, corrosion-resistant, and durable heterogeneous catalysts based on transition metal oxides that can compete with the existing noble metal based catalysts [4–10]. It has been found that cobalt oxides, specifically on gold substrates [CoO<sub>x</sub>/Au(111)], exhibit high catalytic activity towards the OER [11]. Here, the  $\beta$ -CoOOH phase, consisting of an OH layer and an oxygen layer with a cobalt layer sandwiched in between, has shown the biggest potential for catalytic activity, where edge sites seem to be the most reactive [3, 11–13]. However, in order to fully understand and improve the efficiency of these catalysts, it is vital to map out the electronic structure spatially resolved, which in the end governs the chemical reactivity. In this work, we present scanning tunneling microscopy (STM) and spectroscopy (STS) studies of three cobalt oxide island structures, namely, a single bilayer [Co-O/Au(111); Figs. 1(a)–1(c)], a trilayer [O-Co-O/Au(111); Figs. 1(d)–1(f)], and a multilayer [O-Co-O-Co-O/Au(111); see Figs. 1(g)–1(i)]. Earlier studies focused on structural properties, mainly using STM. Their electronic features have also been investigated, but mostly through nonlocally resolved photoemission methods [13, 14], with only one STS study published on the single-bilayer system that did not include the important edge sites [15]. It is

therefore highly relevant to make an in-depth STS study of all three systems to map out the local electronic structure of the different cobalt oxide structures on Au(111). Spatially resolved measurements of the electronic structure will advance the understanding of which sites of the oxides play a relevant role in the catalytic processes. The generalized *d*-band-model points out three important factors to describe surface reactivity: the center of the substrate *d* band relative to the Fermi level, the degree of filling of this band, and the coupling matrix element between adsorbate and substrate *d* states [16–19]. The first two can be measured with STM, which will thus be used to draw simple relations between the local density of states (LDOS) measured by STS and the reactivities of different sites of cobalt oxide islands observed in the literature. The bilayer and multilayer present with a moiré pattern and a corrugation pattern, respectively, together with site-specific fluctuations of the LDOS near the Fermi level  $E_F$ . Our measurements suggest a correlation between topographic and electronic structures on both island types. We find that the edges of these islands have an electronic nature similar to their respective basal planes, except for seemingly reactive edge sites, where a slight increase in the LDOS near  $E_F$  is found. The trilayer is seen to possess a unique topographic and electronic structure, with the basal plane and rough edge sites having different electronic structures. Rough edges of the trilayer islands could be due to missing oxygen atoms leading to uncoordinated cobalt sites. We report a prominent near-zero bias peak (NZBP) on the basal plane and at straight edges. We link the reported enhanced catalytic activity of the trilayer island to its metallic nature with increased LDOS near  $E_F$ , which is also present in a majority of the island edges, and discuss the NZBP's possible role in cobalt oxide based superconductors.

## II. METHODS

STM and STS measurements were carried out using etched tungsten tips on a LT-STM setup by CreaTec Fischer & Co.

<sup>\*</sup>Present address: Department of Quantum Matter Physics, University of Geneva, 24 Quai Ernest-Ansermet, 1211 Geneva 4, Switzerland; andreas.orsted@unige.ch

<sup>†</sup>ld@mp.aau.dk

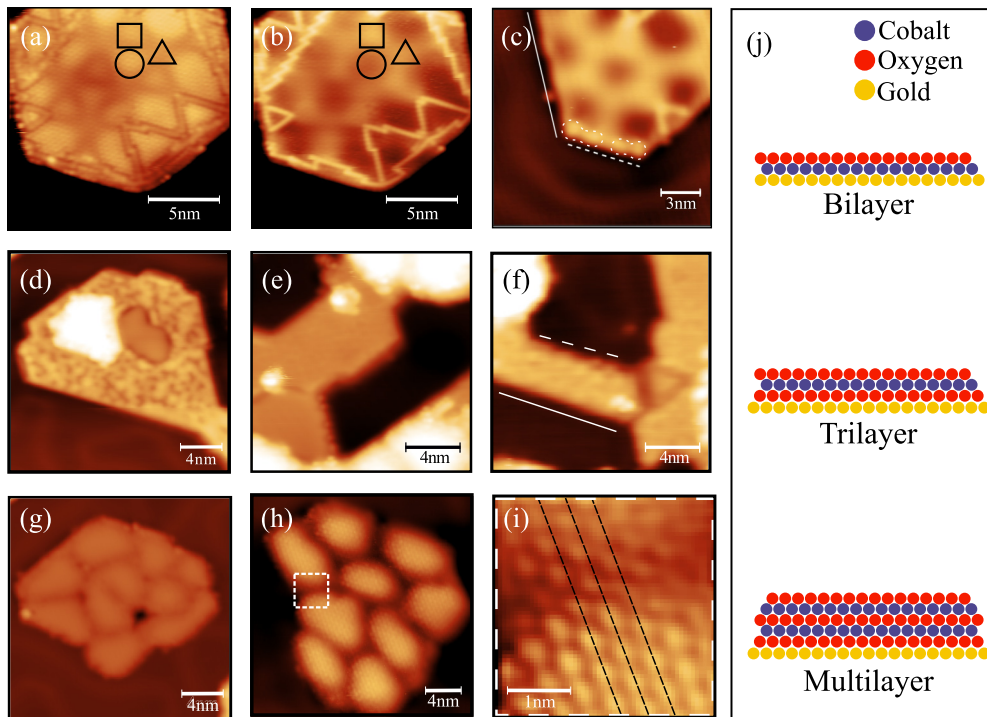


FIG. 1. (a)–(c) show the topography of the single-bilayer structure ( $V_B = 0.25, -0.35, \text{ and } -0.35$  V, respectively). In (a) and (b) the triangle, square, and circle mark fcc, hcp, and TOP sites of the bilayer island. (c) shows a bilayer island with two edges exhibiting slightly different topographies marked by a solid and dashed line. Two other round shapes are indicated by dashed lines in (c), marking slightly elevated regions on this specific bilayer edge. (d)–(f) show three trilayer structures ( $V_B = -0.75, 1.2, \text{ and } 0.7$  V, respectively). (f) shows a narrow patch of the trilayer structure with one straight, even edge marked by a solid line and a more rough uneven edge marked by a dashed line. (g) and (h) show two multilayer islands ( $V_B = -0.75$  and  $0.10$  V, respectively), with (i) being a zoom of the atomic structure of the area marked in (h). (j) shows an illustrative sketch of the layered sandwich structures.

GmbH operated at liquid nitrogen temperatures around 77 K at a base pressure around  $4 \times 10^{-11}$  mbar. STS measurements were performed utilizing the lock-in method with 15–20 mV bias modulations while the tip was in the open feedback loop configuration. The Au(111) single crystal was cleaned through cycles of  $\text{Ar}^+$  ion sputtering and annealing. The tip condition was systematically probed and prepared on the surrounding clean Au(111) crystal prior to any STS investigation of the cobalt oxides. For the oxide growth, cobalt was deposited onto clean Au(111) using an  $e$ -beam evaporator while oxygen pressure was varied using a leak valve and a movable dosing tube to enhance the local pressure at the crystal surface when needed.

### A. Treatment of data

With STS probing the relationship between applied bias voltage and resulting current and conductance ( $I/V$ ) the standard lock-in technique measures the differential tunneling conductance  $dI/dV$ , which can be assumed to be proportional to the LDOS of the sample [20]. The normalized differential tunneling conductance  $(dI/dV)/(I/V)$  is sometimes considered a more precise approximation to the sample LDOS [20]. It presents a number of advantages in comparison to the raw  $dI/dV$  signal and thus is less sensitive to tip-sample distance and work-function variations. Furthermore, dividing  $dI/dV$  by  $I/V$  reduces the otherwise present exponential dependence

found between bias and  $dI/dV$  which may obscure the LDOS features [21]. Treating spectroscopy data in this manner thus provides a more sensitive measure of the electronic landscape for the various cobalt oxides. However, it has been well established that this method breaks down in bias ranges where  $I/V$  goes faster to zero than  $dI/dV$  [20,21]. In this case,  $(dI/dV)/(I/V)$  diverges in a nonphysical manner, which can be handled by a simple low-pass filter on the  $I/V$  term [22,23]. Since some of the cobalt oxides are found to present themselves with such divergences, we have applied the low-pass filter to the  $I/V$  terms throughout this paper. To investigate the spatial variation in the electronic structure on top of the various cobalt oxide islands and across the step edges we perform a series of spectra along well-defined straight lines. The measurement lines are shown in the topography STM images as white arrows, where the direction of the arrow gives the direction of measurement. Typically, 15–30 single spectra are taken along each line at equidistant positions. We perform the normalization on each spectrum and assign values of the  $(dI/dV)/(I/V)$  measurements to different colors such that each singular spectrum can be presented as a one-dimensional multicolored line. Placing these lines one after the other creates the two-dimensional color maps we refer to as line spectra. All figures with line spectra contain a scale bar in arbitrary units of the color coding of the signal intensity. For detailed insight, we also present selected single spectra from each line spectrum. These are termed “cuts” and numbered

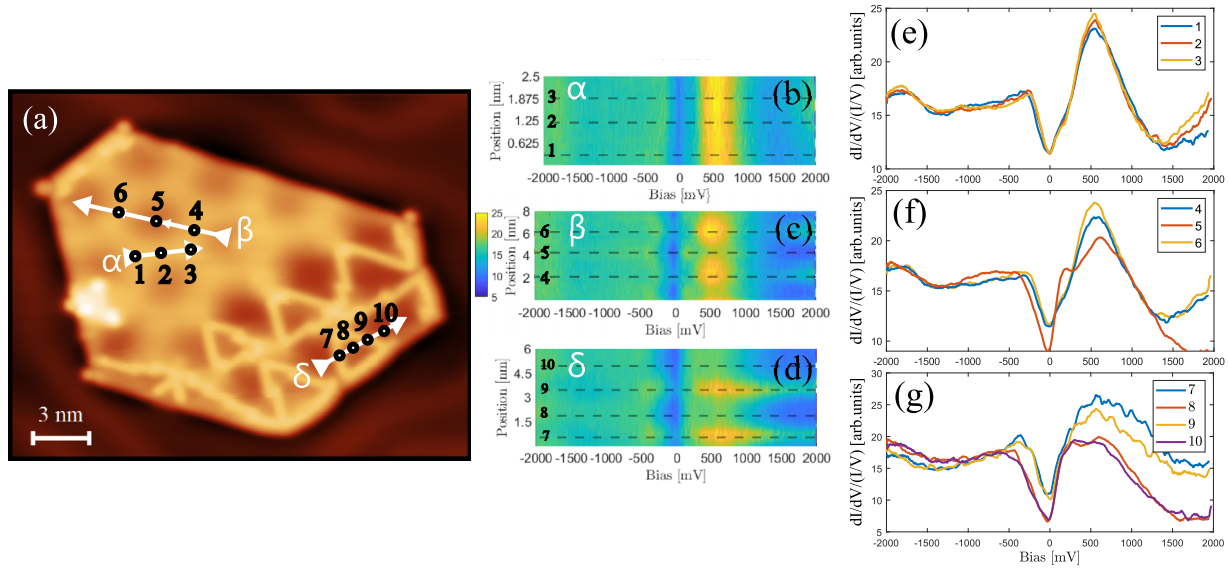


FIG. 2. (a) shows a bilayer topography with defect lines present (bottom right half;  $V_B = -0.75$  V,  $I = 0.1$  nA). Three white arrows labeled  $\alpha$ ,  $\beta$ , and  $\delta$  mark paths followed during line spectra (b)–(d), respectively. (e)–(g) show cross-section cuts from (b)–(d) marked by dashed lines and numbers.

logically such that spectrum number 1 is at the beginning of the arrow/line spectrum.

## B. Island growth and classification

The growth processes of all cobalt oxides investigated are based on the existing literature, and we categorize the various cobalt oxide islands through comparisons of apparent height, moiré structure, and so-called defect lines [5,7,11–13,15,24].

### 1. Bilayer

The single-bilayer cobalt oxide islands [Figs. 1(a) and 1(b)] were grown by depositing cobalt on Au(111) in an oxygen-rich atmosphere at  $2.0 \times 10^{-7}$  mbar with a subsequent postannealing in  $1.0 \times 10^{-7}$  mbar at  $T = 500$  K. We measure an apparent height of  $1.6 \pm 0.2$  Å and observe the characteristic bias-dependent moiré pattern in the topography [5]. In the island basal plane [see Figs. 1(a) and 1(b)] we mark three areas of the moiré with a triangle, a square, and a circle for fcc, hcp, and top-stacking (TOP), which refer to three different atomic stackings [5]. On other parts of the islands several bright lines in the basal plane were observed [see Figs. 1(a)–1(c) and 2(a), bottom right]. These lines are assumed to be excess oxygen adsorbed on the surface layer as an intermediate state between the bilayer and trilayer cobalt oxide [5]. The two main classifications of the edges of bilayer islands are marked by the dashed and solid lines in Fig. 1(c). At negative bias, the edges marked by a solid line have the same apparent height as the fcc and hcp sites of the basal plane, and the edges marked by a dashed line are more irregular and have an apparent height which is higher than the basal plane.

### 2. Trilayer

The trilayer cobalt oxide islands were grown by first depositing cobalt on Au(111) in an oxygen-rich atmosphere at  $2.0 \times 10^{-7}$  mbar followed by postannealing at 400 K at an oxygen pressure of  $1 \times 10^{-6}$  mbar. To further increase the local pressure at the sample, oxygen was supplied through a 6 mm diameter dosing tube placed a few millimeters from the sample surface. The grown islands have an apparent height of  $2.7 \pm 0.2$  Å, and the basal plane exhibits bias dependence, with an inhomogeneous speckled pattern clearly visible in the negative bias range [see Fig. 1(d)], whereas positive bias gives more homogeneous images [see Fig. 1(e)]. These observations are in accordance with the literature [13]. The islands are often found with small patches of multilayer structures growing on top [see Fig. 1(d)]. Two types of edges were found for the trilayer islands, as seen in Fig. 1(f). The edge marked by the solid line has a sharp even termination, and the rough edge marked by the dashed line seems to terminate in a less homogeneous way, going from the basal plane to an apparent height between the basal plane and then to the gold substrate.

### 3. Multilayer

The multilayer islands were synthesized using the same procedure as the one applied for the trilayers, except for slightly higher postannealing temperatures of around 530 K. This results in islands like those seen in Figs. 1(g) and 1(h), with apparent heights of around  $4.8 \pm 0.2$  Å and a very characteristic corrugated pattern that matches the multilayer islands found in the literature, thus confirming the picture of a trilayer island with a bilayer structure on top [13]. In Fig. 1(d) one of these bilayer structures has already nucleated on top of the trilayer island. When the coverage is increased further, nucleation is believed to happen at several locations on the trilayer, and these clusters grow until they complete the multilayer. The basal plane topography can be categorized in



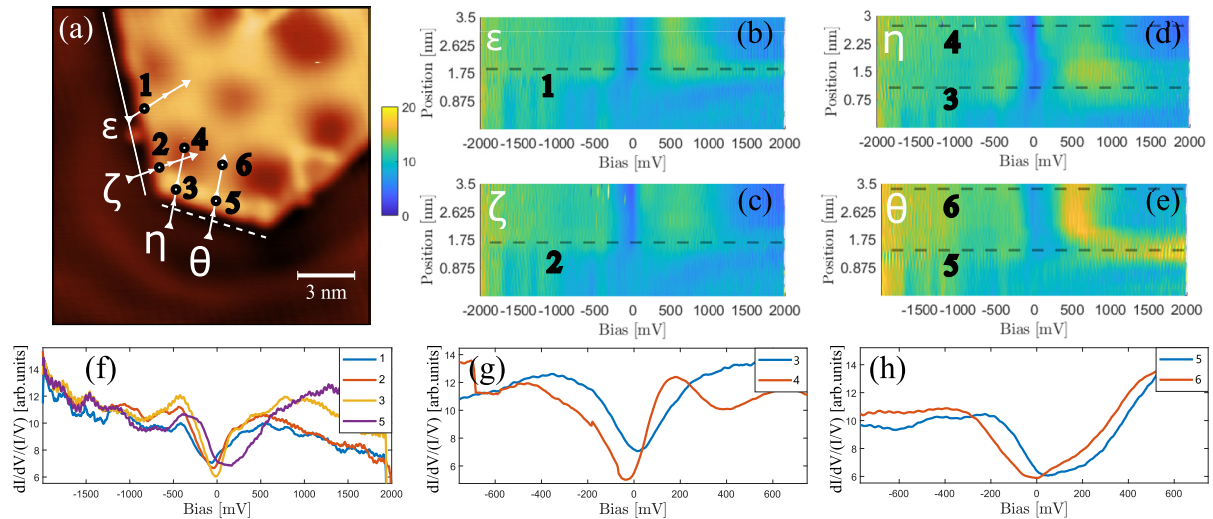


FIG. 3. (a) shows a bilayer topography ( $V_B = -0.75$  V,  $I = 0.1$  nA), with arrows  $\epsilon$ ,  $\zeta$ ,  $\eta$ , and  $\theta$  marking the paths taken during the line scans seen in (b)–(e). The numbers denoted in (a)–(e) correspond to spectra shown in (f)–(h), where (f) shows spectra exactly at the step edges and (g) and (h) each show one spectrum at the step edge (blue) and one on the basal plane (red) to visualize the increased LDOS below  $E_F$  at the edge sites.

three different areas: on top of the clusters, in between two clusters, and, finally, in the junction between three clusters. Looking at the topology of the outer edges of the multilayer islands, they are seen as a brim encasing the collection of clusters making up the island [see Fig. 1(g)]. From a structural point of view, there are two edge cases, one where the edge terminates two clusters and one where the edge terminates a singular cluster. Atomic resolution of this island type reveals a slight shift in the atomic lattice when crossing from one cluster to the next [see Fig. 1(i)]. The mismatch between the atomic rows is in accordance with clusters having nucleated at different locations/sites. For a larger-scale image of the multilayer topography and a zoom, see Fig. 8 in the Appendix. The exact origin of the structure and pattern of the multilayer islands was not further investigated in this study.

### III. RESULTS

#### A. Bilayer

In Fig. 2 three line spectra in representative areas of a bilayer island are presented together with selected single-point spectra cuts. Line spectrum  $\alpha$  going from fcc to hcp [see Figs. 2(a) and 2(b)] reveals the electronic structure of the two stacking orders together with the transition between the two. The line spectra show a reduction in the LDOS around  $E_F$  and one pronounced peak at 0.60 V. There are no significant LDOS variations along line  $\alpha$  in Figs. 2(a) and 2(b), which is also evident from the three selected cuts of the line spectrum shown in Fig. 2(e), with cuts 1, 2, and 3 made at fcc, transition, and hcp sites, respectively. The spectra validate the electronic similarity between fcc and hcp sites. Line spectrum  $\beta$  runs from a TOP site across the fcc/hcp transition sites multiple times [see Figs. 2(a) and 2(c)]. The spectra in these areas [see Figs. 2(c) and 2(f)] show a different LDOS on the TOP site compared to fcc and hcp. The TOP site, corresponding to spectrum 5 in Fig. 2(f), has a greater reduction in the LDOS

near  $E_F$  together with an additional peak near 200 mV and a lower peak intensity at 600 mV compared to the fcc and hcp sites. Furthermore, the LDOS in the far positive bias range is slightly higher for the transition sites compared to the TOP site. Finally, spectroscopic data on areas with defect lines are shown in Figs. 2(a), 2(d) and 2(g). The spectral scan path  $\delta$  crosses from TOP-like sites to defect lines alternately. The defect lines give off a unique spectroscopic signal, while the TOP-like sites show electronic signals similar to that found on the TOP sites, except for a lower peak near 600 mV. The intensity of the occupied states in the region a few hundred millivolts below the Fermi level on the defect lines is greatly enhanced compared to the TOP-like sites with the peak feature on the negative site moved somewhere between  $-400$  and  $-300$  mV while also showing an increased LDOS in the entire positive bias range. In general, the line spectra show that the electronic structure of the basal plane is tightly correlated with the topographical moiré and defect structure. Turning our attention to the bilayer edges (see Fig. 3), the electronic structure is found to be similar to that of the basal plane except for subtle differences such as an intensity reduction of the broad peak at 600 mV and a slight increase in the LDOS in the majority of the bias range, especially at large positive bias but also in the region just below the Fermi level. Looking closely at the spectroscopy, the electronic edges are seen to be highly localized, most clearly seen in Fig. 3(e), where the line spectrum goes from gold to the edge (marked by a dashed line in the line spectrum) onto the usual fcc/hcp spectroscopy. The edges marked by the solid line in Fig. 3(a) have electronic properties almost identical to the basal plane [see Figs. 3(b) and 3(c)], whereas edges marked by the dashed line in Fig. 3(a) are found to possess a shift of the entire electronic structure towards positive bias [see Fig. 3(d) and 3(e)]. Looking more closely at the individual spectra in Fig. 3(f), the edge sites are all found to have a peak around  $-500$  to  $-400$  mV. Furthermore, spectra 1, 2, and 3 follow roughly

the same behavior across the Fermi level, with a broad peak between 500 and 700 mV, whereas spectrum 4 seems slightly shifted towards positive bias, with an increasing LDOS going to higher positive bias. The spectra following  $\theta$  are seen to have marginally increased LDOS at the Fermi level compared to the other spectra [see Fig. 3(f)]. Figures 3(g) and 3(h) compare edge and basal plane spectra from line scans  $\eta$  and  $\theta$ . Here, it is clear that the narrow gap near  $E_F$  in the basal plane is not as pronounced for this specific edge type and that there are more states around and below  $E_F$  for this edge type.

### B. Trilayer

In Figs. 4(a) and 4(b) a trilayer topography and a line spectrum, respectively, are presented. In addition, a line spectrum at a smaller bias range is shown in Fig. 4(c), and four selected single-spectrum cuts are given in Fig. 4(d). The positions of the cuts are marked on the topography and as dashed lines in Fig. 4(b). The most prominent feature of the trilayer spectra is a strong NZBP, with the full width at half maximum of the peaks being approximately 55 mV.<sup>1</sup> This feature is found throughout the entire basal plane, with peak positions around  $E_F$ , shifting from 0 to 40 mV depending on location. The shift is seen to be correlated with topographic variations, where the peak position is towards positive bias for topographically high sites and negative bias for topographically lower sites. Furthermore, topographically low sites show an increased LDOS in the far positive bias range. It is also observed that the intensity of the NZBP is lower in the low sites (spectra 1 and 3) compared to the high sites [spectra 2 and 4; see Figs. 4(b)–4(d)]. In Fig. 4(c), a close-up of the line spectrum seen in Fig. 4(b) shows a seemingly binary peak position jumping between two values. Using a simple automated peak-finding algorithm, we traced the near zero-bias peak in 926 spectra taken on 14 different trilayer islands from several repeated sample preparations. Creating a histogram with the traced peak positions shows that the majority of the NZBPs are distributed very close to the Fermi level at zero bias, while a smaller portion is distributed around +40 mV. The histogram and analysis description are found in Fig. 7 in the Appendix. In Fig. 4(e)–4(i) the trilayer edges and spectra are presented. In general the LDOS at the edge is enhanced in the majority of the bias range, most prominently seen in Fig. 4(i). As introduced earlier, the trilayer island edges either have sharp and well-defined terminations or experience an apparent height that varies along the edge. Typical spectroscopic measurements across a sharp and well-defined edge are seen in Figs. 4(e) and 4(h). Here, the line spectrum shows how the NZBP remains visible until the usual gold surface state is observed as the tip goes from trilayer to gold [top left corner of Fig. 4(h) at around  $-500$  mV]. In the spectra following line spectrum  $\chi$  in Figs. 4(e) and 4(h), a slight elevation of the LDOS is seen in the majority of the negative bias range together with the NZBP. Spectroscopy for the second edge type, where the apparent height is seen to vary, is less well defined [see Figs. 4(f) and 4(i)]. On some

<sup>1</sup>It is noted that the NZBP is also seen in the pure  $dI/dV$  and is thus not an effect of the normalization procedure.

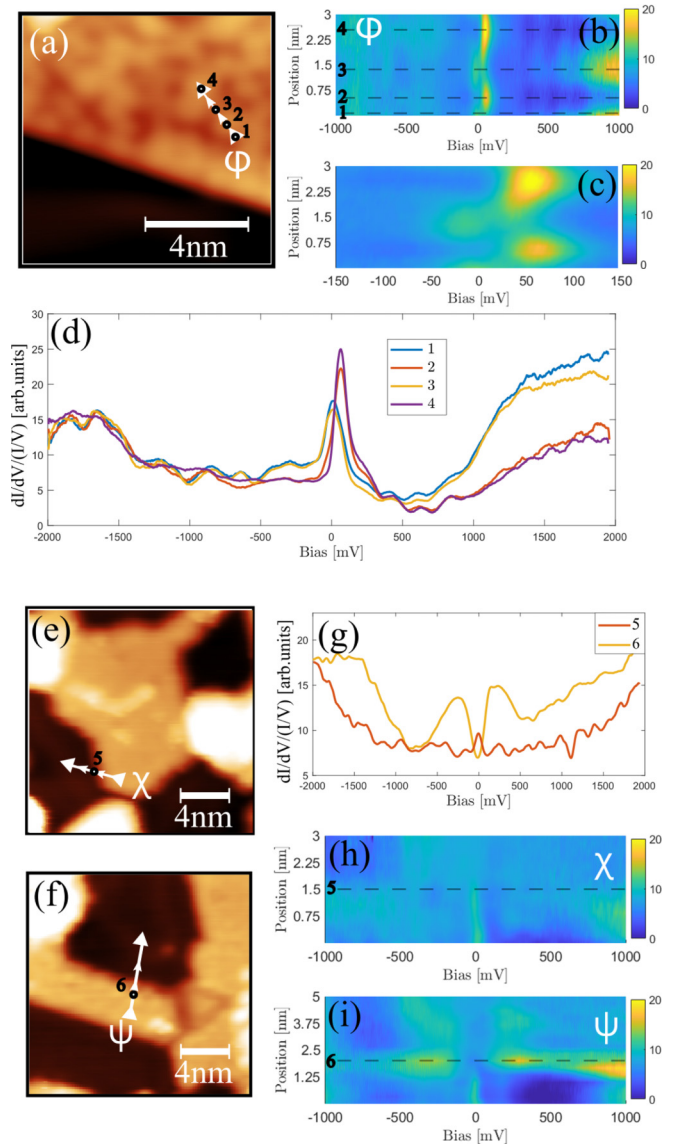


FIG. 4. (a) shows a trilayer topography ( $V_B = -0.75$  V,  $I = 0.1$  nA), with the arrows marking the path taken during the line spectra plot seen in (b). (c) is the same as (b), but with a smaller bias range, with vertical lines guiding the eye for the alternating peak position. (d) shows singular spectra from the line spectra presented in (b). The numbers denoted in (a) and (b) correspond to the spectra shown in (d). (e) and (g) and (f) and (h) present two line spectra performed across two different trilayer edges. Again, the white arrows represent the line spectrum direction, and dashed lines 5 and 6 refer to singular spectra seen in (i).

sites, the spectroscopy is seen to resemble that of the well-defined edge sites, whereas on others the NZBP is suppressed on the edge. In these cases, two broad peaklike features on either side of  $E_F$  at approximately  $\pm 250$  mV are typically observed. Throughout our spectroscopic investigation of this second edge type, we have observed many electronic hybrids between these two cases. We find locations on the uneven edges where the NZBP is present and likewise find seemingly even edges where the NZBP dies out slightly and gives rise to

the two previously mentioned peaks around  $E_F$ . In general, the trilayers are found to show a more metallic behavior, lacking a gap near  $E_F$  compared to the other islands, and edges having a larger LDOS near  $E_F$  compared to the basal plane.

### C. Multilayer

Last, we present the STS measurements of the electronic structure on the multilayer cobalt oxides in Fig. 5. The spectroscopy is found to be highly position dependent, in particular at bias values around and above  $E_F$ . In Fig. 5(b), a line spectrum following path  $\rho$  is shown, where the enumerated dashed lines mark the single spectral cuts shown in Fig. 5(e). The beginning of the line spectrum  $\rho$  is placed at the junction between three clusters. Here, a broad gaplike feature centered around  $E_F$  with a width around 1.2 eV is found [see cut 1 in Fig. 5(e)]. Whereas the negative bias side is rather featureless, the positive bias side experiences a pronounced peak around 1 V. As the scan progresses onto the top of a cluster, the LDOS near  $E_F$  gradually increases, reducing the gaplike feature to a few hundred meV [see cut 2 in Fig. 5(e)]. On the positive bias side of the small gaplike feature, a peak in the LDOS is seen around +200 mV. The LDOS decreases slightly and peaks again around +900 mV. The scan then goes to a junction between two clusters. Here, the gaplike feature width is somewhere in between values from the two previous sites [see cut 3 in Fig. 5(e)]. Spectra across the edges are presented in Figs. 5(c) and 5(d), with single-spectrum cuts at the exact edge positions given in Fig. 5(f). It is clear that the electronic properties mimic those of the junction sites found in the basal plane. The gap around the Fermi level is very evident in the line scans [Figs. 5(c) and 5(d)] and in the spectra taken at the edge positions, shown in Fig. 5(f).

## IV. DISCUSSION

### A. Bilayer

The single-bilayer topography is found to be highly bias dependent, where the moiré pattern changes contrast in STM images depending on the bias [see Figs. 1(a) and 1(b)]. At negative bias, the moiré pattern displays what looks like a hexagonal pattern but presents itself in a more triangular manner using positive bias, similar to a kagomé lattice. Similar features have also been reported elsewhere, where the kagomélike pattern was related to the Co lattice of the island [24]. In Figs. 1(a) and 1(b), the hcp, fcc, and TOP points are marked by the square, circle, and triangle on a single-bilayer cobalt oxide, with each of these sites referring to a specific stacking sequence of the cobalt and oxide layers. The interplay between atomic and electronic structure was probed using STS, with resulting spectra seen in Fig. 2. The distinct differences between the sites' electronic structures become evident through small variations in the LDOS, especially near  $E_F$ . This is also evident through the STM bias dependence across the moiré pattern. The electronic differences between fcc, hcp, and TOP can possibly be explained by varying hybridization between cobalt and gold due to the lattice mismatch [18,25], which in turn leads to a periodic change in charge transfer between the substrate and island [5]. The three sites are very similar electronically but have

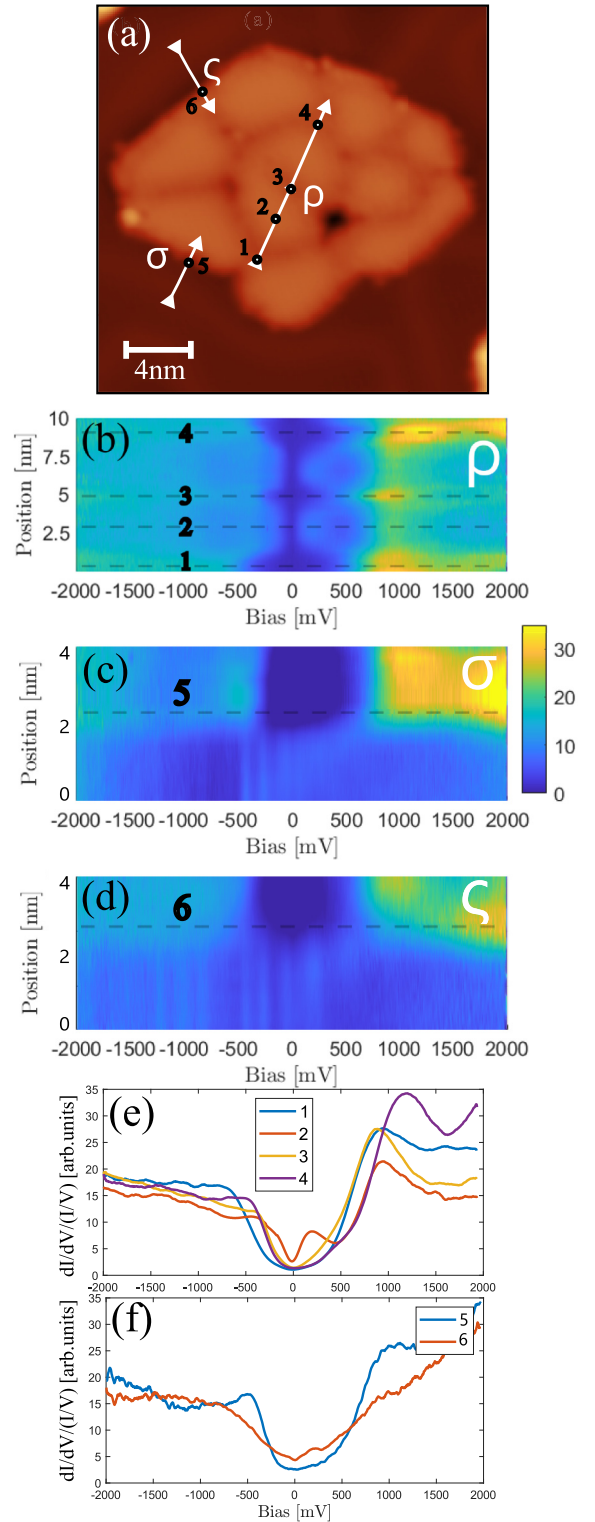


FIG. 5. (a) shows a multilayer topography ( $V_B = -0.75$  V,  $I = 0.3$  nA), with lines  $\rho$ ,  $\sigma$ , and  $\zeta$  marking the paths taken during the line spectra seen in (b)–(d). (e) shows four crosscuts of the line spectrum presented in (b), and (f) shows the spectra taken on two edge sites from (c) and (d).

a few differences. The fcc and hcp sites are largely the same, whereas the TOP sites are found to have a greatly decreased LDOS near  $E_F$  but show a small shoulder near +250 mV. Looking into how the defect lines arrange themselves on the



basal plane, it seems like they tend to form along the fcc to hcp paths, which is most clearly seen in Fig. 1(a), where the defect line is found to follow the triangular geometry of the fcc/hcp sites. The larger LDOS near  $E_F$  may explain this tendency, as increased LDOS near  $E_F$  has been found to be important for activity for oxygen species [26]. It is noted that the current findings agree well with recent STS  $dI/dV$  measurements on various basal plane sites of the interior of the bilayer island [15]. The edges were not investigated. There are some differences in the intensity of the peaks that can be rationalized by the fact that the spectra in Ref. [15] are  $dI/dV$ , whereas the current spectra are normalized  $(dI/dV)/(I/V)$ . When comparing our peak positions in cuts 1–4 and 6 from Fig. 2 with those termed “bright moiré sites” and cut 5 with the “dark moiré sites” [15], we see very good correspondence. A third site termed the “ $\beta$ -region” may be compared with cuts 7 and 9 in Fig. 2. The intensity and location of the peak located around 500 mV in the  $\beta$  region vary strongly across this specific site; however, we do observe the same tendencies of elevated peak intensity around 500 to 700 mV as reported in the literature. The electronic properties of the four investigated edges revealed three almost identical edges on sites 1, 2, and 3 [see Figs. 3(b)–3(d)], with a peak in the LDOS around  $-450$  mV and a broader peaklike feature around 500–600 mV, with some discrepancies. The fourth edge site [see Fig. 3(e)] showed a shifted LDOS compared to the others, with a higher number of occupied states near  $E_F$ . This may thus explain why the edges are the most reactive sites, as observed earlier [11]. Direct comparison of the measured LDOS at basal plane and edge sites confirms this, as shown in Figs. 3(g) and 3(h). Furthermore, the line scan labeled  $\theta$  runs between two regions with slightly higher apparent height compared to the basal plane, similar to that seen in the defect lines. If these higher edge sites are due to oxygen buildup, then  $\theta$  may scan across an exposed high-activity region. That this edge could be more reactive correlates nicely with most of the dashed edge possibly being covered with adatoms, while the edge marked by the solid line is found to lack such adatoms. For more topographic insight into this specific edge, see Fig. 6 in the Appendix. The correlation between the slightly higher LDOS near  $E_F$  and reactivity, although not very pronounced, may be supported by considering the nature of how the oxygen defect line condenses in the basal plane. We see a tendency for the oxygen to nucleate in the areas with the highest LDOS near  $E_F$ , namely, on the hcp and fcc sites [see Figs. 2(a) and 2(c)]. This confirms our suspected correlation between LDOS features near  $E_F$  and the reactivity seen in the exposed edge patch [11].

### B. Trilayer

STM topographies taken at negative bias depict the trilayer cobalt oxides as ruffled structured islands with an irregular pattern. STM in the positive bias reveals a much smoother topography [see Figs. 1(e) and 1(f)]. As seen in Figs. 1(d)–1(f), 4(a), 4(e) and 4(f), the trilayer island has no clear periodic structure or distinct symmetry. The structures observed on the basal planes of these islands have been linked to OH group formation on top of the island, thought to be an effect of the trilayers’ water splitting properties occurring even with

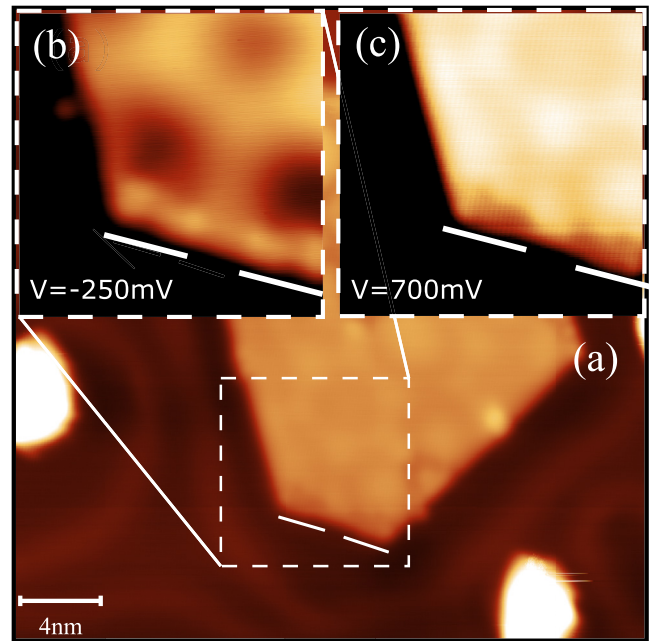


FIG. 6. The bilayer topography presented in Fig. 3 taken with two different biases and changes in color contrast. (a) Large topography taken with 700 mV bias, like the zoom in (b), whereas (c) is taken with  $-250$  mV bias. Small straight lines are inserted to indicate the nature of the island edge.

the small number of water molecules present at UHV [7,13]. From STS measurements taken for both low and high sites of the islands [see Figs. 4(a), 4(c) and 4(d)], we see small differences for spectra taken from the two sites. Here, the bias-dependent topographies and slight electronic differences across the surface may well be explained by a partial OH top layer. The position of the NZBP is seen to shift around 0 to  $+40$  mV and is found to follow high and low areas of the basal plane. This tells us that the shifting peak could simply be explained by adatom effects causing a rigid shift of the band structure by some tens of meV. The rigidity claim here is supported by the fact that all structures in the spectroscopy seem to shift rigidly with the NZBP position. The pronounced NZBP, corresponding to a large LDOS near the Fermi level, provides a very unique electronic fingerprint in the STS of this island. Sharp peaks like these are often ascribed to flat electronic bands, or when they are near the Fermi level, they may point to highly correlated physics such as the Kondo effect. However, Kondo peaks are typically observed in systems with a single magnetic atom on a metal surface at liquid helium temperatures and precisely at zero bias [27–29]. For the current observations at 77 K together with the systematic shifts around  $E_F$  we find it more likely that the peak is related to a flat electronic band near  $E_F$ , where flat bands are known to be responsible for large narrow peaks in STS in many systems [30–33]. Density functional theory (DFT) calculations of the band structure for this system do indeed reveal a rather flat electronic band close to the Fermi level [14]. With the literature anticipating the trilayer islands metal edges to be the most catalytic active sites [3], our findings here showing at least two electronically different terminations of the trilayer edge sites

are important. On the edges marked by a solid line, the NZBP has a tendency to remain all the way to the edge [see Figs. 4(e) and 4(h)], whereas on some of the uneven edges, the NZBP dies out and two broader peaks on either side of  $E_F$  appear [see Figs. 4(f) and 4(i)]. We suspect that highly increased LDOS at  $E_F$  in most of the edges is what causes the trilayer cobalt oxides to show heightened catalytic activity towards the Oxygen reduction reaction (ORR) [34] compared to the other islands. From a spectroscopic point of view, the trilayer edges with an NZBP are the islands with the highest LDOS at the Fermi level, making this specific island edge stand out from the others, mimicking peaks in LDOS near  $E_F$  found in Pt(111) [35–37]. This also fits well with the picture established during our investigation of the single bilayer, where sites with locally increased LDOS at  $E_F$  were found to be favored in oxygen nucleation. In general, as can also be seen in the Appendix, the first few angstroms into the trilayer edges are found to have an enhanced LDOS in the majority of the bias range compared to not only the basal plane of the island but also the gold substrate. It has been well established that an increase in metallicity can be linked to increased catalytic activity. This is seen, for example, in MoS<sub>2</sub>, in which metallic edge sites are found to facilitate catalytic processes [38–40]. The topographic and spectroscopic findings raise the possibility that the uneven edges might correspond to oxygen-deprived trilayer sites, potentially exposing undercoordinated cobalt. It is hypothesized that the abundance of spectroscopic hybrids between the even and uneven edge types of the trilayer could be attributed to varying degrees of oxygen deprivation. These speculations may also be supported by the trilayer growth mechanism proposed in the literature [5]. We would furthermore like to point out an intriguing detail regarding the nature of possible flat bands near  $E_F$  in the context of CoO<sub>2</sub>, namely, the role of trilayer cobalt oxide in the superconductivity of Na<sub>x</sub>CoO<sub>2</sub>·H<sub>2</sub>O [1]. Our findings suggesting a flat band at  $E_F$ , together with prior findings on the related superconductive system Na<sub>x</sub>CoO<sub>2</sub>·H<sub>2</sub>O, may indicate that one driving force [41] for the observed superconductivity found in the LDOS peak near  $E_F$  reported here could be what is commonly referred to as a Van Hove singularity [42]. Other theoretical studies of the trilayer (also called single-layer CoO<sub>2</sub>) suggested features comparable to the ones reported here, where flat bands in the vicinity of the Fermi level in the monolayer are linked to the superconductivity of Na<sub>x</sub>CoO<sub>2</sub>·H<sub>2</sub>O [14,43]. These findings support our claims of superconducting-related LDOS features in the trilayer cobalt oxide.

### C. Multilayer

The multilayer islands are dominated by a strong corrugation, giving the impression of several smaller islands or clusters having merged. Besides geometrical reasons, the lower apparent height between clusters could also be an electronic effect since the width of the gap around  $E_F$  was found to be site dependent. STS measurements on three major sites in the basal plane reveal low-intensity gaps of varying size around zero bias. The gaplike features are widest at the junction between three clusters, narrower between two clusters, and, finally, smallest on top of the clusters, where an extra peaklike feature is seen around +200 mV. We note that

when the cobalt oxides become nanometers thick, a very clear band gap of around 2 eV evolves, as shown in recent STS measurements [44,45]. The overall insulating nature of the multilayer islands agrees well with the low affinity for H<sub>2</sub>O and H<sub>2</sub> dissociative adsorption found in this specific island type [13].

### D. Comparison with photoemission data

A direct comparison of photoemission spectroscopy (PES) and STS is not trivial since the two methods each have their advantages and limitations [20,46]. Besides the fundamental differences in how the electronic structure is probed, PES covers only the occupied states, while STS can measure both below and above the Fermi level, and where PES averages over large areas of the surface, STS provides a very high degree of spatial resolution. Using STM, it is thus possible to clearly distinguish the LDOS contributions of different atomic sites on the surface. Angle-resolved PES (ARPES) has the clear advantage of wave vector resolution and is thus able to measure the band structure, and PES can furthermore cover a much wider range in energies below  $E_F$ . In comparisons, it is noted that positive binding energy in PES corresponds to negative bias (energy) in STS. Valence band measurements of the bilayer, trilayer, and multilayer on Au(111) all show two overlapping features at 0.4 and 0.8 eV binding energy with varying intensities, where the 0.4 eV feature is most intense on the bilayer and the 0.8 eV feature is most intense on the trilayer and multilayer [13]. The present STS data show a maximum at around −0.4 eV bias for the bilayer, both on the basal plane (Fig. 2) and at the edges (Fig. 3). On the multilayer, the STS shows a peaklike feature around −0.4 eV at one of the edges [Fig. 5(f), cut 5]. Also, the basal plane of the multilayer in the junction between the clusters has a similar peaklike feature [see Fig. 5(e), cut 4]. In the case of the trilayer, the only matching peak in STS is that seen in Fig. 4(g) (cut 6) at one of the edges. For the 0.8 eV binding energy peak the only feature we observe throughout our investigation is a broad feature around −0.8 eV bias on the multilayer basal plane [see Fig. 5(e), cut 1]. However, there is, in general, reasonable agreement with the PES data and, furthermore, agreement with the ARPES measurements on the trilayer [14]. In addition to the broad range from  $E_F$  to 0.8 eV binding energy, intensities located around 1.5 eV binding energy were observed as a unique feature of the trilayer [13,14]. The present STS data also show a clear signal at bias values around −1.5 eV [Figs. 4(d) and 4(g), most distinct at the edge, cut 6]. The peak observed at 1.5 eV binding energy attracted attention since it is speculated to possibly play a key role in the catalytic activity reported [13]. Our findings conclude that the edges are, in particular, contributing to the LDOS in this energy range. Finally, we note that the strong NZBP measured by STS is not observed in PES since it is too close to (or even above)  $E_F$ .

## V. CONCLUSION

In summary, we reported an extensive scanning tunneling spectroscopy study of cobalt oxide nanoislands grown on Au(111). Measuring atomically resolved spectra across



the islands allowed us to map out the electronic structures of bilayer, trilayer, and multilayer nanoislands, both in the interior and at the island edges, which are known to be particularly important for applications in catalysis. On the bilayer and multilayer islands we found moderate increases in the LDOS below  $E_F$  at the edges, and on the trilayer island we discovered a large increase in the LDOS, in particular at one kind of edge. In the end, chemical reactivity is governed by the electronic structure, and our results thus contribute to a better understanding of cobalt oxide based catalysts. Furthermore, the discovery of a pervasive near-zero bias peak spanning the entire basal plane of the trilayer island suggests the existence of a remarkably flat electronic band at the Fermi level. This was briefly discussed in relation to recent DFT calculations of the band structure and linked to theoretical predictions of a precursor of superconductivity in  $\text{Na}_x\text{CoO}_2\cdot\text{H}_2\text{O}$ .

### ACKNOWLEDGMENTS

This work was supported by the Danish National Committee for Research Infrastructure (NUFI) through the ESS-Lighthouse Q-MAT.

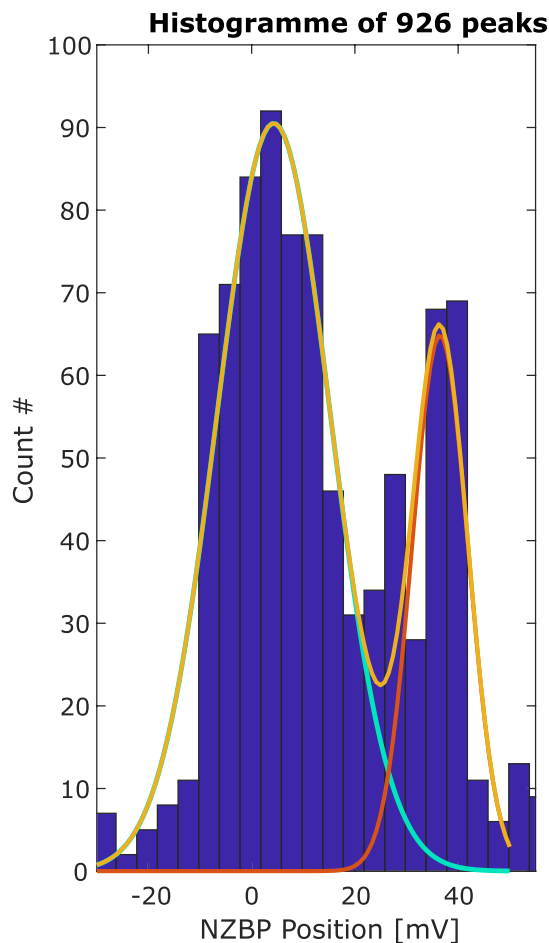


FIG. 7. Histogram of 926 peak traced positions. On top of the histogram is a fit made as a sum of two normal distributions.

## APPENDIX: SUPPORTING INFORMATION FOR UNRAVELING THE ELECTRONIC STRUCTURE OF COBALT OXIDES ON Au(111)

### 1. Bilayer

In Fig. 6 the same topography as presented in Fig. 3 is seen, but with fewer illustrations, allowing us to better see the topography. Here, it is also clear that depending on the probing bias, very different apparent topographies are achieved. The two probing biases show somewhat inverted versions of each other. Focusing on the edge itself, it becomes relatively clear in the 700 mV topography that the edge marked by two solid lines consists of two flavors. At the two lines, topography similar to that of defect lines is seen, and in between a seemingly normal basal plane edge is seen.

### 2. Trilayer

The trilayer structure is found to exhibit relatively simple topographic and electronic variations in the basal plane. The most apparent changes observed are rigid shifts of the entire electronic structure by a few millivolts across apparent high and low sites. In order to understand the behavior of the shift, we analyze the bare zero bias peak movement through histograms. A histogram tracking the NZBP in 926 spectra on the trilayer is given in Fig. 7. From the histogram, it is obvious that there are two distinct peak positions. One is located very close to the Fermi level, and one is shifted towards around 40 mV.

The histogram presented in Fig. 7 was made using a simple peak-finding algorithm in MATLAB. Here, it is important to mention that the function itself can be tuned to be more or less sensitive to small fluctuations in the analyzed data, and we used a set of variables which, in most cases, either managed

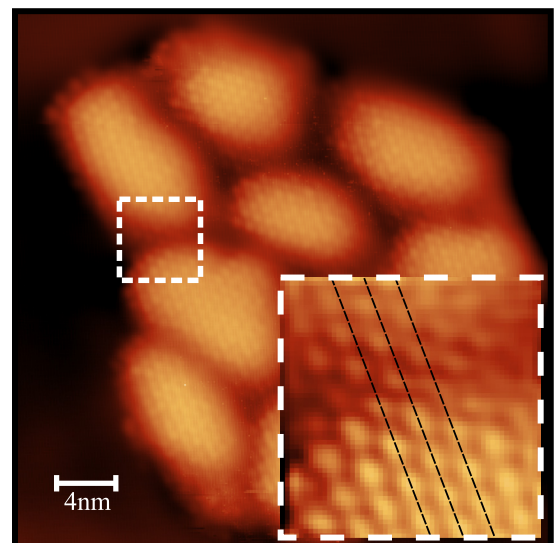


FIG. 8. STM image of an atomically resolved multilayer island with a zoom of a junction part of the island.

to locate the peak without falsely marking small fluctuations as peaks or sometimes did not find the peak. However, of the more than 1400 spectra analyzed, the algorithm found 926 peaks near zero in our data, and we consider the finding relevant, with the histogram being made up of roughly two normal distributions.

### 3. Multilayer

Here, we present a large-scale image of the multilayer island presented in the main text (see Fig. 8). The goal of Fig. 8 is to show a zoomed version of the one found in the main text in order to more clearly illustrate the atomic shift observed during the crossing from one cluster to the next.

- [1] K. Takada, H. Sakurai, E. Takayama-Muromachi, F. Izumi, R. Dilanian, and T. Sasaki, Superconductivity in two-dimensional CoO<sub>2</sub> layers, *Nature (London)* **422**, 53 (2003).
- [2] B. Raveau and M. M. Seikh, Charge ordering in cobalt oxides: Impact on structure, magnetic and transport properties, *J. Inorg. Org. Chem.* **641**, 1385 (2015).
- [3] M. Bajdich, M. Garcia-Mota, A. Vojvodic, J. K. Nørskov, and A. T. Bell, Theoretical investigation of the activity of cobalt oxides for the electrochemical oxidation of water, *J. Am. Chem. Soc.* **135**, 13521 (2013).
- [4] B. S. Yeo and A. T. Bell, Enhanced activity of gold-supported cobalt oxide for the electrochemical evolution of oxygen, *J. Am. Chem. Soc.* **133**, 5587 (2011).
- [5] J. Fester, M. Bajdich, A. S. Walton, Z. Sun, P. N. Plessow, A. Vojvodic, and J. V. Lauritsen, Comparative analysis of cobalt oxide nanoisland stability and edge structures on three related noble metal surfaces: Au(111), Pt(111) and Ag(111), *Top. Catal.* **60**, 503 (2017).
- [6] N. Johansson, L. R. Merte, E. Grånäs, S. Wendt, J. N. Andersen, J. Schnadt, and J. Knudsen, Oxidation of ultrathin FeO(111) grown on Pt(111): Spectroscopic evidence for hydroxylation, *Top. Catal.* **59**, 506 (2016).
- [7] J. Fester, Z. Sun, J. Rodríguez-Fernández, A. Walton, and J. V. Lauritsen, Phase transitions of cobalt oxide bilayers on Au(111) and Pt(111): The role of edge sites and substrate interactions, *J. Phys. Chem. B* **122**, 561 (2018).
- [8] F. Song and X. Hu, Exfoliation of layered double hydroxides for enhanced oxygen evolution catalysis, *Nat. Commun.* **5**, 4477 (2014).
- [9] Q. Fu, W.-X. Li, Y. Yao, H. Liu, H.-Y. Su, D. Ma, X.-K. Gu, L. Chen, Z. Wang, H. Zhang, B. Wang, and X. Bao, Interface-confined ferrous centers for catalytic oxidation, *Science* **328**, 1141 (2010).
- [10] Z. W. Seh, J. Kibsgaard, C. F. Dickens, I. Chorkendorff, J. K. Nørskov, and T. F. Jaramillo, Combining theory and experiment in electrocatalysis: Insights into materials design, *Science* **355**, eaad4998 (2017).
- [11] J. Fester, M. García-Melchor, A. Walton, M. Bajdich, Z. Li, L. Lammich, A. Vojvodic, and J. Lauritsen, Edge reactivity and water-assisted dissociation on cobalt oxide nanoislands, *Nat. Commun.* **8**, 14169 (2017).
- [12] A. S. Walton, J. Fester, M. Bajdich, M. A. Arman, J. Osiecki, J. Knudsen, A. Vojvodic, and J. V. Lauritsen, Interface controlled oxidation states in layered cobalt oxide nanoislands on gold, *ACS Nano* **9**, 2445 (2015).
- [13] J. Fester, A. Walton, Z. Li, and J. V. Lauritsen, Gold-supported two-dimensional cobalt oxyhydroxide (CoOOH) and multilayer cobalt oxide islands, *Phys. Chem. Chem. Phys.* **19**, 2425 (2017).
- [14] A. J. U. Holt, S. Pakdel, J. Rodríguez-Fernández, Y. Zhang, D. Curcio, Z. Sun, P. Lacovig, Y.-X. Yao, J. V. Lauritsen, S. Lizzit *et al.*, Electronic properties of single-layer CoO<sub>2</sub>/Au(111), *2D Mater.* **8**, 035050 (2021).
- [15] A. Sánchez-Grande, H. C. Nguyễn, K. Lauwaet, J. Rodríguez-Fernández, E. Carrasco, B. Cirera, Z. Sun, J. I. Urgel, R. Miranda, J. V. Lauritsen *et al.*, Electrically tunable reactivity of substrate-supported cobalt oxide nanocrystals, *Small* **18**, 2106407 (2022).
- [16] B. Hammer and J. K. Nørskov, Why gold is the noblest of all the metals, *Nature (London)* **376**, 238 (1995).
- [17] B. Hammer, Y. Morikawa, and J. K. Nørskov, CO chemisorption at metal surfaces and overlayers, *Phys. Rev. Lett.* **76**, 2141 (1996).
- [18] A. Ruban, B. Hammer, P. Stoltze, H. Skriver, and J. Nørskov, Surface electronic structure and reactivity of transition and noble metals, *J. Mol. Catal. A: Chem.* **115**, 421 (1997).
- [19] B. Hammer and J. K. Nørskov, Theoretical surface science and catalysis—Calculations and concepts, *Adv. Catal.* **45**, 71 (2000).
- [20] C. J. Chen, *Introduction to Scanning Tunneling Microscopy* (Oxford University Press, Oxford, 2008).
- [21] R. Feenstra, J. A. Stroscio, and A. Fein, Tunneling spectroscopy of the Si(111) 2 × 1 surface, *Surf. Sci.* **181**, 295 (1987).
- [22] P. Mårtensson and R. M. Feenstra, Geometric and electronic structure of antimony on the GaAs(110) surface studied by scanning tunneling microscopy, *Phys. Rev. B* **39**, 7744 (1989).
- [23] F. Ming, D. Mulugeta, W. Tu, T. S. Smith, P. Vilmercati, G. Lee, Y. Huang, R. D. Diehl, P. Snijders, and H. Weitering, Hidden phase in a two-dimensional Sn layer stabilized by modulation hole doping, *Nat. Commun.* **8**, 14721 (2017).
- [24] J. Fester, Z. Sun, J. Rodríguez-Fernández, A. S. Walton, and J. V. Lauritsen, Structure and stability of Au-supported layered cobalt oxide nanoislands in ambient conditions, *J. Phys. Chem. C* **123**, 9176 (2019).
- [25] J. Bork, P. Wahl, L. Diekhöner, and K. Kern, Potential energy landscape of metallic moire patterns, *New J. Phys.* **11**, 113051 (2009).
- [26] C.-E. Kim, D.-H. Lim, J. H. Jang, H. J. Kim, S. P. Yoon, J. Han, S. W. Nam, S.-A. Hong, A. Soon, and H. C. Ham, Effect of gold subsurface layer on the surface activity and segregation in Pt/Au/Pt<sub>3</sub>M (where M= 3 d transition metals) alloy catalyst from first-principles, *J. Chem. Phys.* **142**, 034707 (2015).
- [27] V. Madhavan, W. Chen, T. Jamneala, M. Crommie, and N. Wingreen, Tunneling into a single magnetic atom: Spectroscopic evidence of the Kondo resonance, *Science* **280**, 567 (1998).
- [28] P. Wahl, A. Seitsonen, L. Diekhöner, M. Schneider, and K. Kern, Kondo-effect of substitutional cobalt impurities at copper surfaces, *New J. Phys.* **11**, 113015 (2009).
- [29] C. Ayani, M. Pissara, I. Ibarburu, M. Garnica, R. Miranda, F. Calleja, F. Martin, and A. Vázquez de Parga, Two-dimensional

- Kondo lattice in a TaS<sub>2</sub> van der Waals heterostructure, [arXiv:2205.11383](https://arxiv.org/abs/2205.11383).
- [30] R. Hoffmann, How chemistry and physics meet in the solid state, *Angew. Chem., Int. Ed. Engl.* **26**, 846 (1987).
- [31] Z. Li, J. Zhuang, L. Wang, H. Feng, Q. Gao, X. Xu, W. Hao, X. Wang, C. Zhang, K. Wu, S. X. Dou, L. Chen, Z. Hu, and Y. Du, Realization of flat band with possible nontrivial topology in electronic kagome lattice, *Sci. Adv.* **4**, eaau4511 (2018).
- [32] A. Kerelsky, C. Rubio-Verdú, L. Xian, D. M. Kennes, D. Halbertal, N. Finney, L. Song, S. Turkel, L. Wang, K. Watanabe, T. Taniguchi, J. Hone, C. Dean, D. N. Basov, A. Rubio, and A. N. Pasupathy, Moiréless correlations in ABCA graphene, *Proc. Natl. Acad. Sci. USA* **118**, e2017366118 (2021).
- [33] Z. Zhang, Y. Wang, K. Watanabe, T. Taniguchi, K. Ueno, E. Tutuc, and B. J. LeRoy, Flat bands in twisted bilayer transition metal dichalcogenides, *Nat. Phys.* **16**, 1093 (2020).
- [34] K. Kusada, D. Wu, T. Yamamoto, T. Toriyama, S. Matsumura, W. Xie, M. Koyama, S. Kawaguchi, Y. Kubota, and H. Kitagawa, Emergence of high ORR activity through controlling local density-of-states by alloying immiscible Au and Ir, *Chem. Sci.* **10**, 652 (2019).
- [35] K. Krupski, M. Moors, P. Jóźwik, T. Kobiela, and A. Krupski, Structure determination of Au on Pt(111) surface: LEED, STM and DFT study, *Materials* **8**, 2935 (2015).
- [36] M. Lynch and P. Hu, A density functional theory study of CO and atomic oxygen chemisorption on Pt(111), *Surf. Sci.* **458**, 1 (2000).
- [37] C. Zhang, R. Baxter, P. Hu, A. Alavi, and M.-H. Lee, A density functional theory study of carbon monoxide oxidation on the Cu<sub>3</sub> Pt(111) alloy surface: Comparison with the reactions on Pt(111) and Cu(111), *J. Chem. Phys.* **115**, 5272 (2001).
- [38] M. A. Lukowski, A. S. Daniel, F. Meng, A. Forticaux, L. Li, and S. Jin, Enhanced hydrogen evolution catalysis from chemically exfoliated metallic MoS<sub>2</sub> nanosheets, *J. Am. Chem. Soc.* **135**, 10274 (2013).
- [39] D. Voiry, M. Salehi, R. Silva, T. Fujita, M. Chen, T. Asefa, V. B. Shenoy, G. Eda, and M. Chhowalla, Conducting MoS<sub>2</sub> nanosheets as catalysts for hydrogen evolution reaction, *Nano Lett.* **13**, 6222 (2013).
- [40] T. F. Jaramillo, K. P. Jørgensen, J. Bonde, J. H. Nielsen, S. Horch, and I. Chorkendorff, Identification of active edge sites for electrochemical H<sub>2</sub> evolution from MoS<sub>2</sub> nanocatalysts, *Science* **317**, 100 (2007).
- [41] S. Peotta and P. Törmä, Superfluidity in topologically nontrivial flat bands, *Nat. Commun.* **6**, 8944 (2015).
- [42] D. Yudin, D. Hirschmeier, H. Hafermann, O. Eriksson, A. I. Lichtenstein, and M. I. Katsnelson, Fermi condensation near Van Hove singularities within the Hubbard model on the triangular lattice, *Phys. Rev. Lett.* **112**, 070403 (2014).
- [43] D.-L. Nguyen, C.-R. Hsingl, and C.-M. Wei, Theoretical prediction of superconductivity in monolayer CoO<sub>2</sub>, *Nanoscale* **11**, 17052 (2019).
- [44] M. Ammon, S. Baumann, T. Kißlinger, J. Rieger, T. Fauster, J. Redinger, L. Hammer, and M. A. Schneider, Epitaxial cobalt oxide films with wurtzite structure on Au(111), *Phys. Status Solidi RRL* **15**, 2100383 (2021).
- [45] M. Ammon, A. Raabgrund, and M. A. Schneider, Adsorption, self-assembly and self-metalation of tetra-cyanophenyl porphyrins on semiconducting CoO(100) films, *Surf. Sci.* **720**, 122044 (2022).
- [46] S. Hüfner, *Photoelectron Spectroscopy: Principles and Applications* (Springer, Berlin-Heidelberg, 2003).